Eclipsed X-ray Bursts from Magnetar SGR J1935+2154 and the Fireball Measurements

SHENG-LUN XIE , ^{1,2} A-MING CHEN , ^{1,3} YUN-WEI YU , ^{1,3} SHAO-LIN XIONG , ² HUA FENG , ² SHUANG-NAN ZHANG , ^{2,4} ZI-GAO DAI , ⁵ WANG-CHEN XUE , ^{2,4} MING-YU GE, ² XIAO-BO LI, ² LIANG-DUAN LIU , ^{1,3} JIA-CONG LIU , ^{2,4} WEN-JUN TAN, ^{2,4} CHEN-WEI WANG , ^{2,4} SHU-XU YI, ² PENG ZHANG, ^{2,6} YAN-QIU ZHANG , ^{2,4} ZHEN ZHANG, ² CHAO ZHENG , ^{2,4} AND XIAO-PING ZHENG , ³

¹Institute of Astrophysics, Central China Normal University, Wuhan 430079, China
²State Key Laboratory of Particle Astrophysics, Institute of High Energy Physics, Chinese Academy of Sciences, 19B Yuquan Road, Beijing 100049, China

³Education Research and Application Center, National Astronomical Data Center, Wuhan 430079, China

⁴University of Chinese Academy of Sciences, Beijing 100049, China

⁵ Department of Astronomy, School of Physical Sciences, University of Science and Technology of China, Hefei 230026, China ⁶ College of Electronic and Information Engineering, Tongji University, Shanghai 201804, China

ABSTRACT

X-ray bursts from the magnetar can lead to the formation of fireballs trapped by the magnetic field and co-rotating with the star. The fireball emission could occasionally be eclipsed by the magnetar, especially when the burst duration is comparable to the magnetar's spin period. In this work, we discover a peculiar type of burst whose light curve has a plateau-like feature among the long bursts of the magnetar SGR J1935+2154. Based on these bursts, we identified four burst candidates with eclipse-like characteristics. By fitting their light curves with the eclipse fireball model, the viewing angle of the magnetar relative to its spin axis is estimated to be $17^{\circ} \pm 10^{\circ}$. The distances from the fireballs to the magnetar are found to be more than five times the magnetar's radius, indicating that the fireballs are suspended in the magnetosphere rather than adhering to the magnetar surface. We also find this configuration is well consistent with the implication of the cyclotron resonance scattering feature in their spectra. Our results suggest that some intermediate X-ray bursts of SGR 1935+2154 may originate from magnetic reconnection within the magnetosphere rather than the starquake.

Keywords: Magnetars (992) — Soft gamma-ray repeaters (1471) — Astronomy data analysis (1858)

1. INTRODUCTION

Magnetars are a subclass of neutron stars with extremely high magnetic fields $(10^{14} \sim 10^{15} \text{ G})$, which usually exhibit as pulsars/bursters of long spin periods $(2 \sim 10 \text{ s})$ and high spin-down rates $(10^{-13} \sim 10^{-11} \text{ s} \cdot \text{s}^{-1})$ in our Galaxy (P. M. Woods & C. Thompson 2006a; V. M. Kaspi 2010; S. Mereghetti 2013; S. A. Olausen & V. M. Kaspi 2014; V. M. Kaspi & A. M. Beloborodov 2017; M. Negro et al. 2024). These objects are well-known for their bursting and flaring activity, during which the luminosity of the neutron stars rises suddenly in X-rays and soft gamma-rays. The bright X-ray/gamma-ray transients from magnetars are usually classified into different subtypes in terms of their timescales and energetics, including ordinary short bursts, intermediate burst/flares, and giant flares (J. F. Olive et al. 2004; P. M. Woods & C. Thompson 2006b; S. Mereghetti 2008; G. L. Israel et al. 2008). The short bursts are most common, typically have a duration of 0.1 - 1 s and a peak luminosity in the range of $10^{39} \sim 10^{41} \text{ erg} \cdot \text{s}^{-1}$. The giant flares are rare events, generally start with a short $(0.1 \sim 0.2 \text{ s})$ spike of hard X-rays with peak luminosity $(10^{44} \sim 10^{47} \text{ erg} \cdot \text{s}^{-1})$ followed by a softer pulsating tail lasting a few minutes. So far, only a total number of three

Corresponding author: Yun-Wei Yu

yuyw@ccnu.edu.cn

Corresponding author: Shao-Lin Xiong

xiongsl@ihep.ac.cn

giant flares have been discovered in our Galaxy, while some new candidates have recently been claimed to be detected from extra-galaxies (e.g., GRB 231115A from M82, GRB 070222 from M83, and GRB 180128A and GRB 200415A from NGC 253, S. Mereghetti et al. 2024; A. C. Trigg et al. 2024; O. J. Roberts et al. 2021; E. Burns et al. 2021). The intermediate bursts/flares exhibit properties with durations, luminosities, and releasing energies between short bursts and giant flares. Moreover, they typically have abrupt onset and endpoints, with duration timescales shorter than the spin periods. Besides, in some so-called outburst events, the X-ray emission of magnetars can suddenly rise to be $10 \sim 10^3$ times brighter than their quiescent level and, subsequently, decay in weeks to months/years as a power-law or exponential behavior (e.g.F. Coti Zelati et al. 2018). The total energy released from an outburst is typically in the range of $10^{41} \sim 10^{43}$ erg. The onsets of outbursts are usually associated with one or more ordinary bursts, but their precise relationship is still unclear.

The prevailing explanation behind the magnetar bursts/flares is that large amounts of energy stored in magnetic fields are released due to a rapid change in the magnetic field structure and strength, given that the rotational energy of magnetars is always too low to explain the observations. Such a scenario is strongly supported by the fact that the X-ray luminosity of magnetars is positively correlated with the strength of their magnetic fields (C. Thompson et al. 2000, 2002; D. A. Uzdensky 2011; K. Parfrey et al. 2013). Magnetic fields distributed in the magnetosphere of magnetars are believed to be more complicated (e.g., twisted) than those of normal pulsars (C. Thompson & R. C. Duncan 1995; C. Thompson & O. Blaes 1998), even though the global structure of the fields is still generally dipolar. Therefore, the magnetar surface can be persistently heated due to the gradual untwisting of the field lines, resulting in a higher temperature than normal pulsars. The most concerning question is what physical processes trigger the burst activities. Some plausible mechanisms have been proposed, such as magnetic stress-induced starquakes (C. Thompson & R. C. Duncan 1995; P. B. Jones 2003; Y. Levin & M. Lyutikov 2012) and magnetic field reconnections of some ropes in the magnetosphere (R. C. Duncan & C. Thompson 1992; Y. Masada et al. 2010; C. Yu 2011; C. Yu & L. Huang 2013; Y. Meng et al. 2014), which lead to sudden changes in the configuration of either internal or external magnetic fields.

Observational constraints on the radiation mechanisms of magnetar bursts are usually derived from their spectral information (e.g., E. GöğüS et al. 1999; E. Göğüs et al. 2000; A. J. van der Horst et al. 2012). In contrast, the light curves of bursts are usually ignored because of their complexity, except for the afterglow emission of some giant flares and outbursts (P. M. Woods et al. 2001; Y. Lyubarsky et al. 2002; X. Li & A. M. Beloborodov 2015). The emission region of a giant flare (probably a fireball consisting of hot electron/positron plasma) is usually suggested to be near the stellar surface and even capable of engulfing the entire magnetar C. Thompson & R. C. Duncan (1995). Therefore, the temporal evolution of the tail emission of flares can show a periodic modulation at the spin period as the fireball co-rotates with the magnetar. The modulations are believed to arise from the inhomogeneous distribution of the fireball relative to the magnetar. However, for relatively normal bursts, including the short and intermediate ones, the corresponding fireballs could be much smaller (if they are still near the stellar surface) and, in any case, only located on one side of the magnetar. Then, it is suggested here that, for these fireballs, we would have a chance to discover an eclipse signal from their light curves if their duration can be comparable to the magnetar's spin period. As illustrated in Figure 1, the fireball emission could be obscured by the magnetar for a period when the fireball moves into the shadow of the magnetar. Such a situation, if it can be discovered, particularly from intermediate bursts, would enable us to constrain the fireball's size and its geometrical relationship with the magnetar and further help to distinguish the different burst-triggering mechanisms.

In this Letter, we aim to search for eclipse-like features in the X-ray bursts of the magnetar SGR J1935+2154 and develop a geometric model to interpret these light curves. Using GECAM and Fermi/GBM data, we identify several long bursts showing plateau-like profiles and perform eclipse model fittings to constrain the viewing angle and fireball distances. These results provide new insights into the spatial configuration of magnetar fireballs and their possible origin. Section 2 describes the eclipse X-ray bursts from SGR J1935+2154, including the data analysis and model fittings. Section 3 presents the discussion and summary of our results. The details of data reduction and spectral analysis are presented in Appendix A and B, respectively.

2. ECLIPSE X-RAY BURSTS

Our attention in this letter is focused on the observations of the magnetar SGR J1935+2154, which is one of the most active magnetars (e.g., G. L. Israel et al. 2016; L. Lin et al. 2020b,a; G. Younes et al. 2020; A. Ridnaia et al. 2021; A. Borghese et al. 2022; C. Cai et al. 2022) and, in particular, has been found to host mysterious fast radio

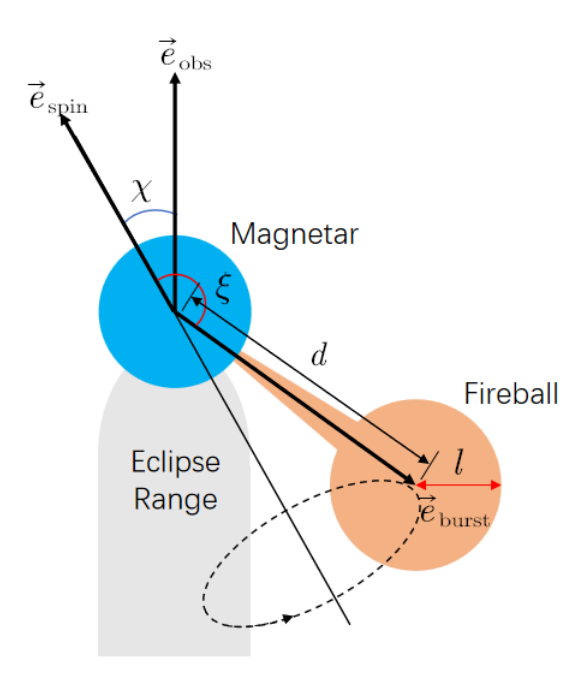


Figure 1. Illustration of the eclipse geometry of a fireball co-rotating with the magnetar.

bursts (FRBs) (C. D. Bochenek et al. 2020; CHIME/FRB Collaboration et al. 2020; C. K. Li et al. 2021). Since the first discovery by Swift Burst Alert Telescope (Swift/BAT) in 2014 (M. Stamatikos et al. 2014), SGR J1935+2154 has attracted a great number of observations including the monitors of Fermi Gamma-ray Burst Monitor (Fermi/GBM) and Gravitational wave high-energy Electromagnetic Counterpart All-sky Monitor (GECAM) (L. Lin et al. 2020b,a; Y. Kaneko et al. 2021; S.-L. Xie et al. 2022; N. u. S. Rehan & A. I. Ibrahim 2023, 2024; S.-L. Xie et al. 2025; N. S. Rehan & A. I. Ibrahim 2025). Up to the end of 2022, Fermi/GBM and GECAM have detected 440 and 256 bursts, respectively, most of which are typical short bursts of a single or multiple peaks. Some statistical studies have been implemented on the distributions of the bursts' energy, duration, and waiting times, from which a particularity of the burst activity hosting the FRB emission had been found (S.-L. Xie et al. 2024; N. S. Rehan & A. I. Ibrahim 2025).

In Figure 2, we display the duration distribution of the total 696 bursts, which determines a mean value of approximately 100 ms. According to the spin period of $P \sim 3.24$ s of SGR J1935+2154, we tentatively take 800 ms (approximately one-fourth of the spin period) as a criterion and obtained 23 bursts above this line. Unfortunately, the light curves of these relatively long bursts usually have complicated multiple peaks, making it difficult to judge whether these light curves are modulated by the eclipse effect. A method is proposed to explore the eclipse effect as follows. Firstly, find out whether there is a specific light curve pattern that could be intrinsic to a group of bursts. Secondly, search for eclipse signals from the bursts that are partially different from the supposed standard pattern.

2.1. Data Analysis

For GECAM and GBM, detectors with source angles $\leq 50^{\circ}$ were selected, and the energy channels affected by the absorption edges (30 \sim 40 keV) were excluded. Further details of the data reduction procedures are provided in Appendix A. Based on the cleaned and calibrated data, we then carry out time-resolved spectral analysis to explore the spectral evolution of the selected long bursts. Background spectra are estimated from pre- and post-burst intervals using low-order polynomial fits. The spectra are grouped to ensure sufficient counts per channel and fitted using maximum-likelihood statistics implemented. Further details of the spectral analysis, including the fitting methods and model comparisons, are summarized in Appendix B.

From the intermediate bursts of SGR J1935+2154, we have indeed found several particular bursts which have a roughly plateau light curve except for the rapid beginning and ending phases (rise and decay). The most representative one is the burst occurring at $t_0 = 2016$ -06-26T13:54:30.720 (labeled as Burst A), as shown in the left panel of Figure 3. Such a plateau indicates that the emission region of this burst probably has a nearly fixed configuration, i.e., the fireball is probably in a dynamic equilibrium.

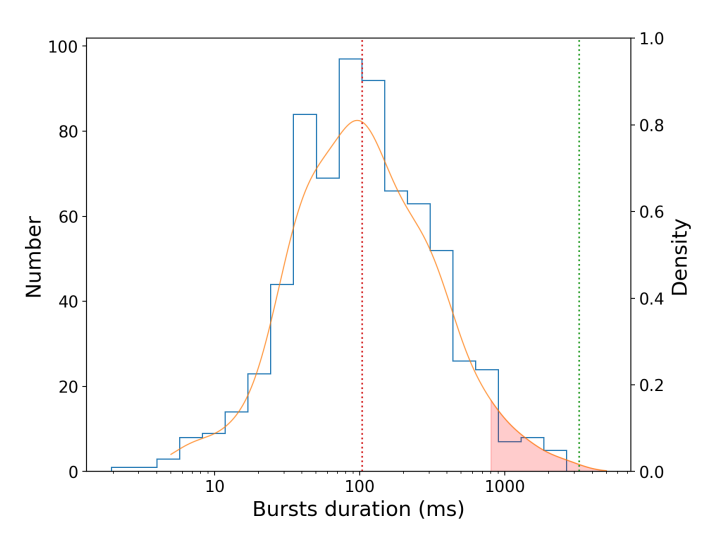


Figure 2. The histogram (blue line) and kernel density (orange line) of the duration distribution of the 696 X-ray bursts from SGR J1935+2154 detected by Fermi/GBM (L. Lin et al. 2020b,a; Y. Kaneko et al. 2021; N. u. S. Rehan & A. I. Ibrahim 2023, 2024) and GECAM (S.-L. Xie et al. 2022, 2025) up to the end of 2022. The red and green vertical dot lines represent the mean value (104.12 ms) of burst duration and the spin period (3.24 s) of SGR J1935+2154, respectively. The duration range where we search for the candidates of eclipsed X-ray bursts is highlighted by the shade.

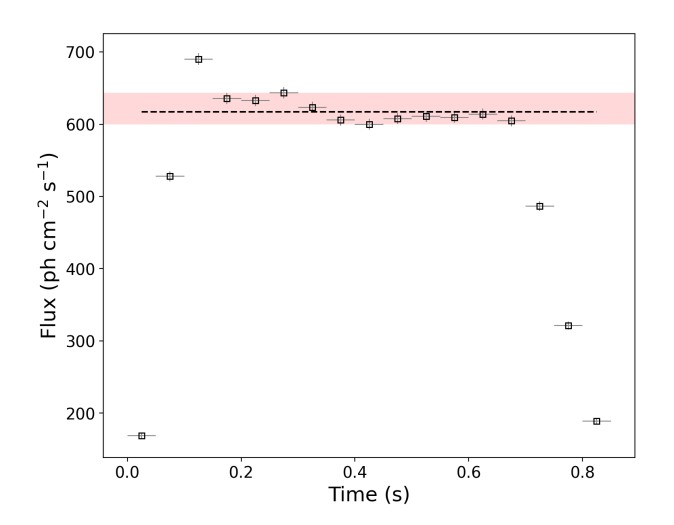
We first tested several spectral models, including a single blackbody (BB), a two-blackbody (BB + BB), and a BB with a cyclotron resonant scattering feature (CRSF). For the representative plateau burst (Burst A), the temperature of a single BB model fluctuates slightly around a constant value, indicating that the slight differences among the spectra could stem from the dynamic fluctuation of the steady fireball. However a clear residual dip appears at $20 \sim 50$ keV (see the Figure B2 in Appendix B), indicating the presence of an absorption feature. Adopting a unified temperature at $k_{\rm B}T=9.49$ keV and introducing a CRSF component at $E_{\rm cyc}=35.0$ keV significantly improves the fit (see the Table B1 in Appendix B for comparison of the AIC/BIC values), suggesting a magnetic field strength much lower than the surface value of the magnetar, i.e., $\sim 3 \times 10^{12}$ G. This indicates that the line-forming region is far away from the surface. Generally speaking, in addition to the black body component, wider-band spectra of X-ray bursts of magnetars sometimes have another spectral component arising from the Comptonization of the thermal photons (K. Ioka 2020; Y.-P. Yang & B. Zhang 2021; S. Yamasaki et al. 2022; Z. J. Zhang et al. 2023), usually dominating the higher energy band ($\gtrsim 80$ keV). This component is not considered here. In summary, from a qualitative perspective, the BB + CRSF model provides a better statistical and physical description of the data, as supported by the AIC and BIC tests. Therefore, the plateau emission of constant temperature and emission area undoubtedly provides us with a special opportunity to explore the eclipse effect.

2.2. Eclipse Modeling

Taking Burst A as a template, we identify four bursts showing similar behaviors to that of Burst A, but with a partial deletion, labeled as Bursts B-E. The light curves of these four bursts are shown in Figure 4, where the rapid rise and decline phases are not fully displayed to more clearly show the details of the plausible 'plateau phase'. The spectral fittings of these bursts reveal a non-evolving temperature but a varying emission area, which can be naturally explained by the eclipse effect due to the emission fireball moving into the shadow of the magnetar. Based on the scenario illustrated in Figure 1, as a zeroth-order approximation, we treat the emission regions of the X-ray bursts as a spherical fireball co-rotating with the magnetar, although their realistic geometrical structure can be much more complicated. We introduce a reference frame with the z-axis towards the observer, i.e., $\vec{e}_{\text{obs}} = (0,0,1)$, and the x-axis in the plane of the observer and the magnetar's spin axis. Therefore, the unit vectors of the spin axis and the fireball can be given by:

$$\vec{e}_{\rm spin} = (\sin \chi, 0, \cos \chi) \,, \tag{1}$$

$$\vec{e}_{\text{burst}} = (\sin \chi \cos \xi - \cos \chi \sin \xi \cos \gamma, \sin \xi \sin \gamma, \cos \chi \cos \xi + \sin \chi \sin \xi \cos \gamma), \tag{2}$$



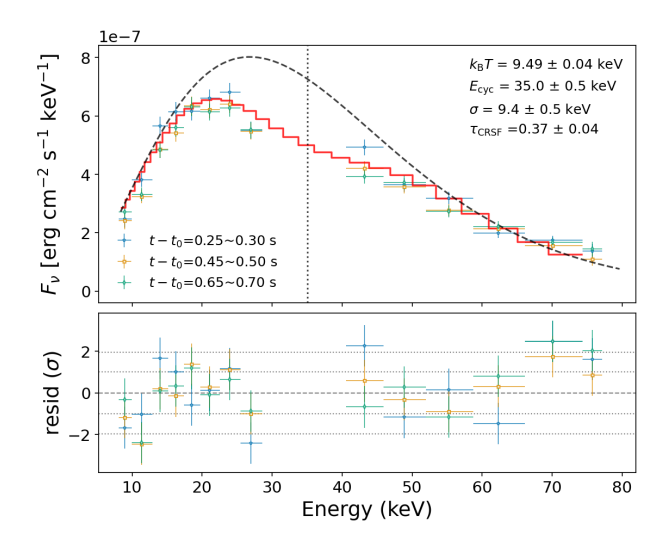


Figure 3. Left: The light curve of a plateau burst observed by Fermi/GBM at 2016-06-26 13:54:30.720 (labeled Burst A), where the dashed line represents the average of the plateau flux, and the fluctuation, as shown by the shaded band, is no more than $\sim 6\%$ of the average. Right: The time-resolved spectra of Burst A, which can be fitted by a non-evolving black body with a CRSF absorption (the red solid histogram). The residuals of the spectral fit are plotted in the lower panel. The dashed line represents the unabsorbed black body. The center of the CRSF line is labeled by the vertical dotted line, while the optical depth τ_{CRSF} and width σ of the absorption are given in the legend.

where χ is the angle between the observer and the spin axis and ξ is the angle between the spin axis and the fireball. Since the fireball co-rotates with the magnetar, the vector \vec{e}_{burst} rotates around \vec{e}_{spin} . Therefore, the rotational phase is given by $\gamma(t) = \Omega t + \phi$, with $\Omega = 2\pi/P$ and ϕ being related to the choice of zero-time during each burst.

We denote θ as the angle between the fireball and the observer (i.e., $\cos\theta = \vec{e}_{\rm burst} \cdot \vec{e}_{\rm obs}$), which varies from $|\chi - \xi|$ to $|\chi + \xi|$ as the fireball co-rotates with the magnetar. For a given pair of angles χ and ξ that satisfy with $|\chi + \xi| \leq \pi/2$ or $|\chi + \xi| \geq 3\pi/2$, the magnetar itself would not eclipse the fireball emission and the emitting area is given by $A_{\rm obs} = \pi l^2$, where l is the radius of the fireball. The eclipse process occurs when $\pi/2 < |\chi + \xi| < 3\pi/2$, and the visible area is determined by the apparent distance between the fireball and the magnetar $\rho = d\cos(\theta - \pi/2)$ as:

$$A_{\text{obs}} = \begin{cases} \pi l^2, & \rho > l + R_{\text{ns}}, \\ \pi l^2 - \Delta A_1 - \Delta A_2, & (l + R_{\text{ns}}) > \rho > \sqrt{l^2 - R_{\text{ns}}^2}, \\ \pi l^2 - \pi R_{\text{ns}}^2 + \Delta A_2 - \Delta A_1, & \sqrt{l^2 - R_{\text{ns}}^2} > \rho > (l - R_{\text{ns}}), \\ \pi l^2 - \pi R_{\text{ns}}^2, & (l - R_{\text{ns}}) > \rho, \end{cases}$$
(3)

where d is the distance of the fireball to the center of the magnetar, ΔA_1 and ΔA_2 are the areas of a portion of circles cut by a line segment, which are given by the angles subtended by the line segment as:

$$\Delta A_1 = \frac{1}{2}l^2 \left(\theta_1 - \sin \theta_1\right), \quad \theta_1 = 2\arccos\left(\frac{l^2 + \rho^2 - R_{\rm ns}^2}{2\rho l}\right),\tag{4}$$

$$\Delta A_2 = \frac{1}{2} R_{\rm ns}^2 \left(\theta_2 - \sin \theta_2 \right), \quad \theta_2 = 2 \arccos \left(\frac{R_{\rm ns}^2 + \rho^2 - l^2}{2\rho R_{\rm ns}} \right).$$
 (5)

Therefore, it is straightforward to define the eclipse factor as:

$$f_e = \frac{A_{\text{obs}}}{\pi l^2}. (6)$$

For the selected bursts, we assume their emitting flux to be constant except for the fast rising and decay phases. Specifically, we write the intrinsic light curve as follows:

$$F_{\text{int}} = F_p \times \Theta(t - t_1) \Theta(t_2 - t), \qquad (7)$$

Table 1. The observational data utilized and the eclipse model fitting parameters. The errors are given at the 1σ confidence level. The symbols l, d, χ , and ξ are defined as illustrated in Figure 1. ϕ is the phase corresponding to the starting time, $R_{\rm ns}$ is the radius of the magnetar, and $F_{\rm p}$ is the peak flux of the bursts.

Labeled burst	A	В	С	D	E	
Start time	2016-06-26	2020-04-27	2020-04-27	2021-12-24	2022-01-14	
	13:54:30.720	18:32:41.640	20:15:20.770	03:42:34.341	20:21:05.500	
Instrument	GBM	$_{ m GBM}$	$_{\mathrm{GBM}}$	$_{ m GBM}$	GECAM-B	
Detectors	n6, n9	n6, n9	n2, n9, na	n1, n3, n5	g1,g6,g7	
Energy (keV)	8-80	8-80	8-80	8-80	20-80	
Duration (s)	0.84	2.15	1.09	1.3	1.5	
Fireball radius (km)	$17.44^{+0.45}_{-0.23}$	$17.58^{+0.63}_{-4.61}$	$19.08^{+2.05}_{-1.67}$	$19.88^{+0.59}_{-1.54}$	$17.32^{+0.42}_{-5.50}$	
Model parameters	Priors	Posteriors				
$\chi \text{ (deg)}$	[0 - 180]	$17.46^{+8.99}_{-6.87}$	$17.11^{+9.69}_{-8.94}$	$18.54^{+15.65}_{-8.16}$	$8.04^{+5.39}_{-3.56}$	
ξ (deg)	[0 - 180]	$155.92^{+9.35}_{-11.71}$	$162.22^{+7.31}_{-9.20}$	$149.38^{+13.22}_{-23.41}$	$172.00^{+3.50}_{-5.43}$	
ϕ (deg)	[0 - 360]	$163.75^{+1.09}_{-1.00}$	$117.60^{+0.33}_{-0.32}$	$136.85^{+0.66}_{-0.69}$	$94.27^{+1.15}_{-1.22}$	
$d/R_{ m ns}$	[1 - 50]	$5.38^{+3.19}_{-1.58}$	$7.65^{+5.01}_{-2.53}$	$8.23^{+5.89}_{-3.15}$	$7.96^{+6.07}_{-3.09}$	
$F_{\rm p} \; ({\rm ph} \; {\rm cm}^{-2} \; {\rm s}^{-1})$	[1 - 1000]	$727.62^{+1.81}_{-1.78}$	$609.91^{+5.21}_{-5.02}$	$601.81^{+2.51}_{-2.58}$	$731.18^{+8.95}_{-12.48}$	
$\chi^2/{ m dof}$	_	14.78/34	27.25/13	15.94/13	75.76/19	

where t_1 and t_2 are the starting and ending times of the burst plateau, F_p is the peak fluxes of each burst, and $\Theta(t)$ is the step function. Therefore, the observed flux is simply given by

$$F_{\text{obs}} = f_e \times F_{\text{int}}.$$
 (8)

Then, fitting the observed light curves of the eclipsed bursts can constrain the position and size of the emitting fireball. We fit the light curves of the four selected bursts, assuming an intrinsically steady fireball, as shown by the dashed lines in Figure 4, with the corresponding posterior distributions shown in Figure 5. The corresponding parameter values with errors are listed in Table 1. In calculations, the intrinsic radii of the fireballs are taken beforehand according to the spectral fittings. The viewing angles derived from the four eclipsed bursts are found to be all concentrated around a common value ⁷ of $\bar{\chi} = 17^{\circ} \pm 10^{\circ}$, as shown in Figure 6, indicating the self-consistency of our modeling. It is further established that the pulsar (neutron star) viewing angle can be determined through a novel eclipse-based method, in contrast to the conventional rotating vector model which relies on radio polarization measurements. The results further show that $d \gg R_{\rm ns}$ and $d \gg l$, which indicate the emitted fireballs of these bursts are far away from but do not adhere to the magnetar's surface. This is consistent with the implication of the CRSFs. Finally, the distance d is much smaller than the radius of the light cylinder as $R_{\rm LC} = cP/2\pi = 1.5 \times 10^5$ km, suggesting that the fireballs are located deep in the magnetosphere.

Note that, in our model, we do not take into account the gravitational lensing effect for simplicity, which can somewhat increase the brightness of a distant light source if the light can graze near the surface of the magnetar. However, given that the fireball is comparable to or several times larger than the magnetar in size, we should treat the fireball as an extended source rather than a point. In such a case, since different differential elements on the source have different distances to the caustic, the magnification of the total brightness of the fireball would be averaged over the entire extended surface. As a result, the brightness variation arising from the distance change of the fireball to the caustic would be much smaller than that observed for a point source (S. Dall'Osso et al. 2024).

3. DISCUSSION AND SUMMARY

The distance measurements of the fireballs to the magnetar surface provide a very stringent constraint on the trigger mechanism of the bursts. Generally speaking, highly twisted magnetic fields in the magnetosphere of magnetars are very likely to extend from the stellar interior, where the toroidal component could dominate. In other words, the energy release of magnetars is ultimately a result of the diffusion of magnetic helicity from the interior to the exterior.

$$\bar{\chi} = \frac{1}{4} \sum_{i=B}^{E} \bar{\chi}_i, \quad \sigma^2 = \frac{1}{4} \sum_{i=B}^{E} \left[\sigma_i^2 + (\bar{\chi}_i - \bar{\chi})^2 \right],$$
 (9)

where $\bar{\chi}_{i=B,...E}$ and σ_i^2 is the posterior mean and variance of *i*-th burst, respectively.

⁷ The common value is estimated from the mean of individual posteriors and includes uncertainties,

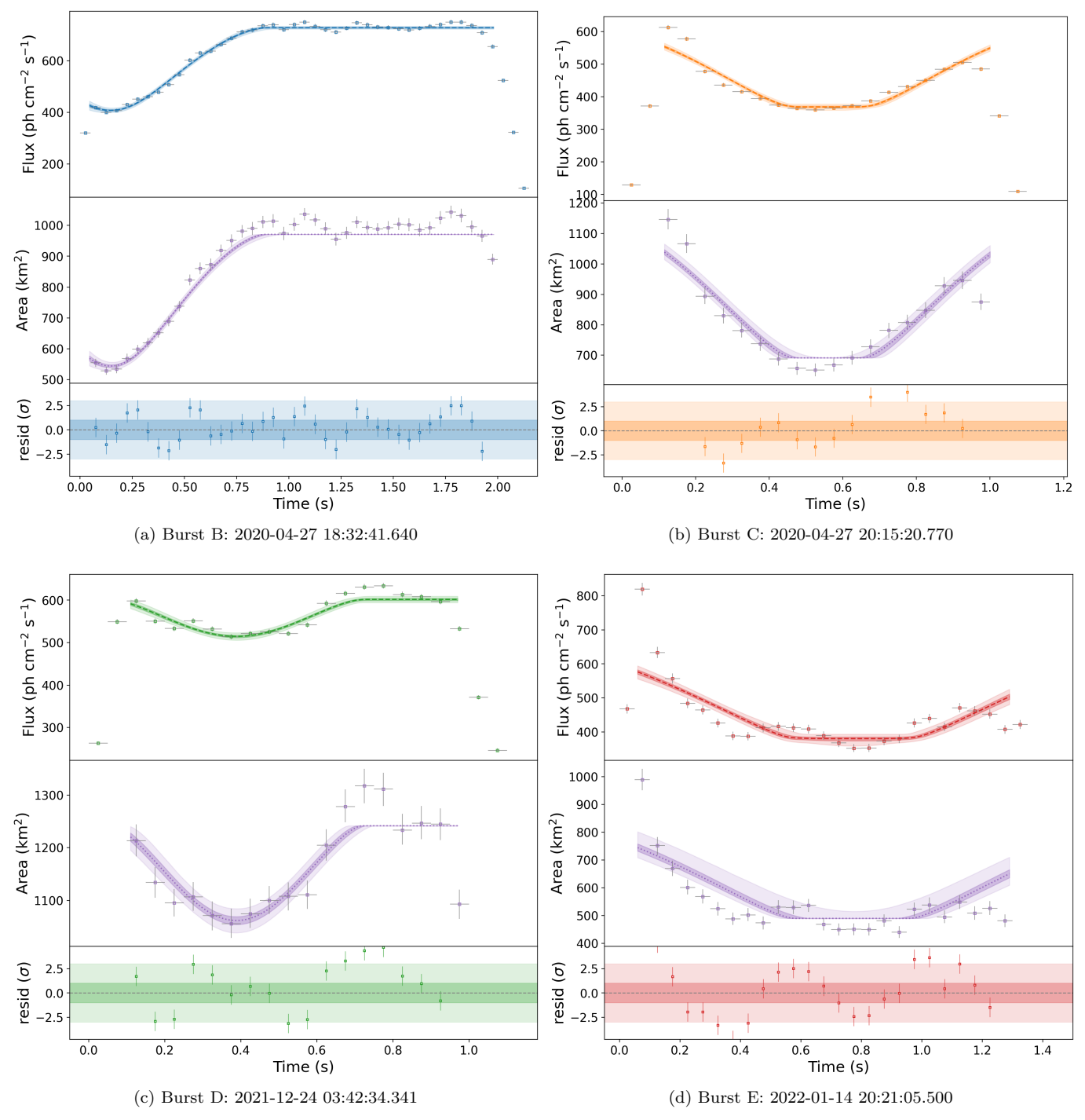


Figure 4. The temporal evolution behaviors of the eclipsed bursts during the plateau phase. The top panels present the evolution of the emission flux, where the dashed lines provide the fittings of these light curves with the eclipse model. In the middle panels, we plot the model-predicted evolutions of the black body emission areas (dotted line), in comparison with the data derived from the fittings of the time-resolved spectra. The residuals of the light curve fittings are shown in the bottom panels, there the shadows represent 1σ and 3σ confidence levels.

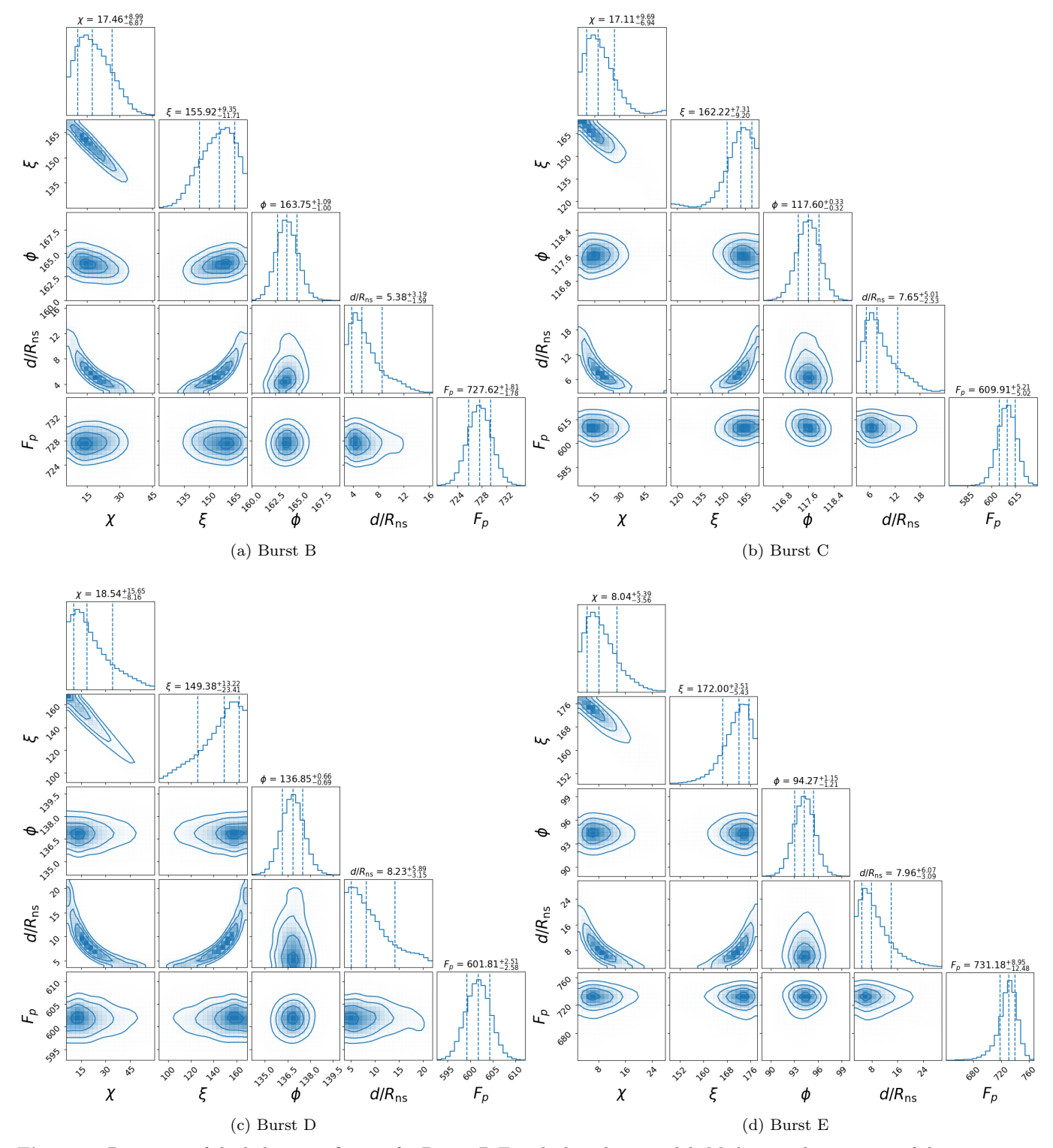


Figure 5. Posteriors of the light curve fittings for Bursts B-E with the eclipse model. Medians and 1 σ ranges of the parameters are labeled.

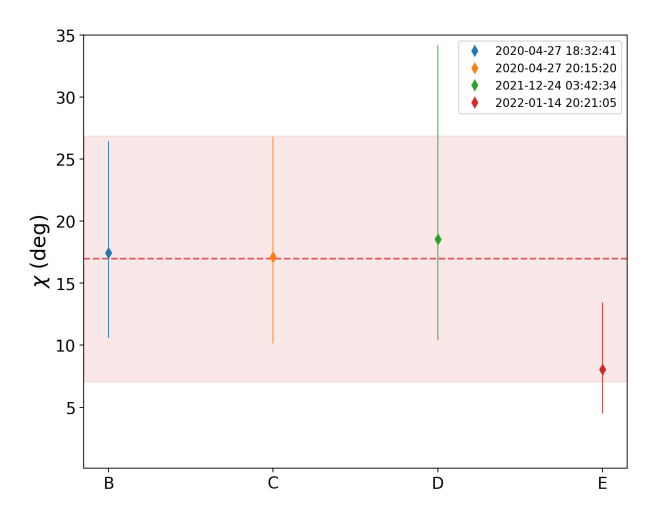


Figure 6. The inferred viewing angle χ of the line of sight relative to the magnetar's spin axis. The dashed line and shaded band show the mean and standard deviation of the four independent measurements.

The connection between the internal and external fields exerts vast stress on the solid crust of magnetar. Then, along with the spin-down of magnetar, the shear stress is gradually accumulated to finally exceed the yield limit of the crust, leading to plastic deformation of the crust and triggering a starquake. In principle, the released strain energy can heat the deforming crustal region, leading to the formation of a hot spot and even a fireball trapped by local magnetic field loops near the surface. However, such a picture is now disfavored for these eclipsed plateau bursts, as their distances are about five times larger than the stellar radius. Instead, the fireballs are inferred to be suspended in the magnetosphere, suggesting them to originate from local magnetic reconnection of some magnetic ropes/knots in the magnetosphere. The magnetic ropes/knots may form as the cumulative product of long-term crustal deformation. Thus, the occurrence of such catastrophic magnetic reconnection is not necessarily linked to an individual starquake, even though the energy released ultimately derives from the cumulative effect of numerous previous starquakes.

In more detail, we can envision the following physical scenario. As a magnetic reconnection occurs in the magnetosphere, an energy of about $E_{\rm iso} \sim 10^{41}$ erg can be released suddenly. Then, a great number of electron and positron pairs can be excited in the reconnection zone and flow into a larger scale region, forming of a freely and adiabatically expanded fireball. The number density of the fireball can be given by (L. D. Landau & E. M. Lifshitz 1980; C. Thompson & R. C. Duncan 1995)

$$n_{\pm} = \frac{1}{2} \left(\frac{2m_{\rm e}k_{\rm B}T_{\rm in}}{\pi\hbar^2} \right)^{3/2} \exp\left(-\frac{m_{\rm e}c^2}{k_{\rm B}T_{\rm in}} \right),$$
 (10)

where the internal temperature of the fireball $T_{\rm in}$ can be roughly estimated to be $k_{\rm B}T_{\rm in}=k_{\rm B}(3E_{\rm iso}/4\pi l^3a)^{1/4}=68(E_{\rm iso}/10^{41}{\rm erg})^{1/4}(l/20{\rm km})^{-3/4}{\rm keV}$ with a being the radiation constant. The fireball expansion could be quickly suppressed if the pressure of the surrounding large-scale magnetic fields can finally exceed the thermal pressure of the fireball, which requires $B\gtrsim 1.6\times 10^{11}~(l/20~{\rm km})^{-3/2}(E_{\rm iso}/10^{41}~{\rm erg})^{1/2}~{\rm G}$ (C. Thompson & R. C. Duncan 1995). By using a simple dipolar field configuration, the field strength at the distance d can be estimated to $B(d)\sim 3.0\times 10^{12}(d/50~{\rm km})^{-3}{\rm G}$, which is obviously strong enough to stop the fireball expansion, where a reference stellar radius $R_{\rm ns}=12~{\rm km}$ is adopted and the surface field strength is taken as $B_{\rm p}=2.2\times 10^{14}{\rm G}$ (G. L. Israel et al. 2016). Therefore, the fireball can finally be trapped by the magnetic fields and suspended in the magnetosphere for a period.

The rationality of a suspended fireball may also be understood from the perspective of interpreting the key properties of the CRSF absorption, including its central energy, line width, and absorption depth. (i) With the magnetic field strength at a reference distance of 50 km, we can determine the position of the first harmonic of CRSFs in the spectra of the bursts as: $E_{\rm cyc} = \hbar e B/m_{\rm e} c = 35.3 \, (d/50 \, {\rm km})^{-3} \, {\rm keV}$, where e and $m_{\rm e}$ are respectively the charge and mass of electrons, c is the speed of light, and the used formula is valid for the case of $B \ll B_{\rm c} = 4.4 \times 10^{13} \, {\rm G}$ with $B_{\rm c}$ being the critical value for Landau quantization. Although very simple, this estimate of $E_{\rm cyc}$ can be very consistent with the values obtained from the spectral fittings, further indicating the self-consistency of the model. However, strictly speaking, some inconsistencies still exit, since the fireball distances inferred from the light curve fittings (see

Table 1) are actually somewhat different from the reference value. Here, the crux of the problem may lie in the complication of the magnetic field configuration of the magnetar, which distinguishes it from the traditional dipolar scenario and complicates the determination of both B(d) and E_{cvc} at a given distance. (ii) It is expected that the widths of CRSF is at least larger than that determined by the Doppler effect as (P. Meszaros & W. Nagel 1985; A. K. Harding & J. K. Daugherty 1991; O. Nishimura 2003; G. Schönherr et al. 2007): $\sigma = (k_{\rm B}T/m_{\rm e}c^2)^{1/2}E_{\rm cyc}|\cos\theta| =$ $4.9 \text{keV} (k_{\text{B}}T/10 \text{keV})^{1/2} (E_{\text{cvc}}/35 \text{keV}) |\cos\theta|$, where θ is the angle between the photon direction and the magnetic field vector. This value is smaller than, but of the same order of magnitude as, the CRSF widths derived from the spectral fittings. However, since the fireball is actually distributed within a spatial range of a few tens of kilometers, the magnetic field strength in the vicinity of the fireball should at least vary on an amplitude of $[(d+l)/(d-l)]^3$. Given this significant variation in the field strength, it would be not surprising to observe a CRSF line a few times broader than the Doppler broadening. (iii) In the outer region adjacent to the fireball surface where the CRSF could be formed, the column density of electrons and positrons can be estimated by $\mu n_{\rm GJ}\Delta$, where μ is the multiplicity, $n_{\rm GJ} = \Omega B/(2\pi ce)$ is the Goldreich-Julian density, and Δ is the thickness of this line-formation region. Then, following Reference J. C. L. Wang et al. (1993), the optical depth of the CRSF absorption can be expressed as $\tau_{\text{CRSF}} =$ $0.3 (\mu/10^3) (\Delta/5 \text{km}) (k_B T/10 \text{keV})^{-1/2}$, which could provide a basic explanation for the optical depths derived from the spectral fittings.

Finally, the dynamical evolution of a fireball is determined by the competition between the internal thermal pressure and external magnetic pressure. Supposing that a burst is triggered impulsively, a plateau emission would occur during a pressure balance. Then, as the majority of the internal energy of the fireball is lost, the balance would be disrupted, and thus the plateau emission ceases. Therefore, we can express the duration of the plateau emission in terms of the diffusion timescale of thermal photons in the fireball as

$$t_{\text{diff}} \sim \frac{l^2}{\lambda} = 3.3 \times 10^4 \left(\frac{k_{\text{B}}T_{\text{in}}}{1 \text{keV}}\right)^{3/2} \exp\left(-\frac{511 \text{keV}}{k_{\text{B}}T_{\text{in}}}\right) \text{ s},\tag{11}$$

where $\lambda = 1/(\sigma_{\rm T} n_{+})$ is the mean free path of the thermal photons with $\sigma_{\rm T}$ being the Thomson cross section and l=20km is adopted for giving the numerical coefficient. However, this timescale is very sensitive to the determination of the internal temperature of the fireball because of the presence of the exponential term. Specifically, by solving equation $t_{\rm diff} \sim 1$ s, we can obtain $k_{\rm B}T_{\rm in} = 32.7$ keV for l = 20 km, which is lower than that inferred from the average internal energy density. Here, it should be noted that the actual temperature within the fireball must exhibit a decreasing distribution from the inside out, which is determined by thermal transfer within the fireball. Given this, it is not surprising to obtain different temperatures from different estimation methods, not to mention that these approaches are rather crude. Then, undoubtedly, a precise calculation of the burst duration requires a detailed characterization of the thermal diffusion. In addition, more complexity can arise from the unclear trigger mechanism of the bursts. Given the complication of locally twisted magnetic fields, magnetic reconnection is likely to occur repeatedly and with complicated dynamical behavior rather than impulsively as supposed above. In this case, the pressure balance of the fireball cannot keep steady and, thus, an evolving and even multi-peaked light curve rather than a plateau would be obtained. Such complicated bursts can be easily found from the longest bursts of SGR J1935+2154, with a larger number than plateau bursts. Since we cannot know the dynamical evolution of the fireballs of these complicated bursts, it is actually impossible to identify eclipse candidates from them, even though their spectral properties are not obviously different from the plateau ones. Furthermore, it is indicated that plateau bursts are actually very rare, which seems sound because of their strict requirement on the burst trigger mechanism. In any case, these facts make it difficult for us to verify the eclipse model from the perspective of number statistics.

ACKNOWLEDGMENTS

This work is supported by the National Key R&D Program of China (2021YFA0718500), the National SKA Program of China (2020SKA0120300), the National Natural Science Foundation of China (grant Nos. 12393811, 12393812, and 12273042), the Strategic Priority Research Program, the Chinese Academy of Sciences (Grant No. XDA30050000, XDB0550300). The GECAM (HuaiRou-1) mission is supported by the Strategic Priority Research Program on Space Science of the Chinese Academy of Sciences.

Facilities: Fermi(GBM), GECAM(B)

APPENDIX

A. DATA REDUCTION

Gravitational wave high-energy Electromagnetic Counterpart All-sky Monitor (GECAM, X. Li et al. 2021; S. Xiao et al. 2022) is originally a constellation of two small X-ray and gamma-ray all-sky observatories funded by the Chinese Academy of Sciences. These two microsatellites, denoted as GECAM-A and GECAM-B, were launched in December 2020. Each GECAM satellite is equipped with 25 Gamma-ray detectors (GRDs) and 8 Charged Particle Detectors (CPDs). Each GRD operates in two readout channels: high gain (HG, 20–300 keV) and low gain (LG, 300 keV–5 MeV), which are independent in terms of data processing, transmission, and dead time. The time resolution of GRDs is 0.1 μ s. We select detectors with detector-to-source angles of $\leq 50^{\circ}$ in our analysis. Given the dominated emission energy range of magnetar bursts ($\leq 100 \text{ keV}$), we focus on using the HG channel for data analysis. The GECAM data reduction tool is GECAMTools ⁸. Considering the lanthanum absorption edge at 38.89 keV for LaBr3, as this feature potentially leads to systematic uncertainties in spectra, we have ignored the data in the range of 35-40 keV (J.-J. He et al. 2023).

Fermi Gamma-ray Burst Monitor (GBM, C. Meegan et al. 2009) has a continuous broadband energy coverage which consists of 12 NaI detectors (8-1000 keV) and 2 Bismuth Germanate (BGO) detectors (0.2-40 MeV). GBM provides three kinds of science data: CSPEC with continuous high energy resolution (1024 ms and 128 energy channels), CTIME with continuous high time resolution (64 ms and 8 energy channels), and TTE (time tagged photon event) with temporal resolution 2 μs and energy resolution 128 channels. We choose the detectors with good detector-to-source angles ($\leq 50^{\circ}$), and hence the highest signal-to-noise ratio A. C. Collazzi et al. (2015); L. Lin et al. (2020b). The data reduction tool used to generate light curves and spectral data is GBM Data Tools (A. Goldstein et al. 2022). Response files are generated by GBM Response Generator v1.13 for spectral analysis. Similar to GECAM, we excluded 30-40 keV data for NaI detectors to avoid the iodine K-edge at 33.17 keV (E. Bissaldi et al. 2009).

B. SPECTRAL ANALYSIS

We process the GECAM event-by-event (EVT) data and GBM TTE data to generate spectral data for 50 ms timeresolved spectral analysis using a data reduction tool. Background spectra are generated from data events in pre- and post-burst time intervals (from t_0 -10 s to t_0 -5 s, and from t_0 +5 s to t_0 +10 s, where t_0 is the burst time), and fitted with a polynomial function to model the background during the burst. Subsequently, this background would be subtracted from the total spectrum in the spectral fitting process. The raw light curves of the five selected bursts, with a 5 ms time resolution and the estimated background level, are shown in Figure B1. These light curves are very unlikely to result from the simple superposition of multiple pulses, although some nontrivial substructures may still exist.

The software elisa is employed for exploring and analyzing the spectral data (W.-C. Xue et al. 2024). In performing maximum likelihood fitting, the χ^2 -statistics are used as a likelihood value to be minimized, and spectral channels are grouped to ensure a minimum of one count per channel for the validity of the fit statistic. Furthermore, to evaluate the performance of different spectral models, we used two commonly adopted information criteria: the Akaike Information Criterion (AIC) and the Bayesian Information Criterion (BIC) (A. R. Liddle 2007). Both criteria balance the goodness of fit and the complexity of the model, penalizing models with more free parameters. Lower AIC or BIC values indicate a more statistically favored model.

First of all, we perform spectral fits for the representative plateau of Burst A, by using four different spectral models. The first model is a single black body (BB), which is written as

$$N(E) = \frac{A_{\text{obs}}}{D_{10}^2} \times \frac{3.29 \times 10^{-4} E^2}{\exp(E/k_{\text{B}}T) - 1},\tag{B1}$$

where $k_{\rm B}T$ is the observed temperature in units of keV, $A_{\rm obs}$ is the observed emission area in km² and D_{10} is the distance to the source in units of 10 kpc. The distance of SGR J1935+2154 with $D \simeq 9$ kpc is adopted (S.-Q. Zhong et al. 2020). This model involves the fewest assumptions. Our analysis shows that the BB temperature fluctuates slightly around a constant value. This temperature variation may result from statistical fluctuations caused by insufficient

⁸ https://github.com/zhangpeng-sci/GECAMTools-Public

photon counts, or alternatively, it could stem from the dynamical fluctuations of the fireball. In any case, based on the assumption of a light-curve plateau, we further consider ignoring these fluctuations, directly assuming a constant temperature, and using this temperature to perform a joint fitting of time-resolved spectra during the plateau phase (i.e., the temperatures are tied (shared) across different time intervals). The logarithm of the likelihood for the joint fitting is defined as

$$\ln \mathcal{L} = \sum_{i} \ln L_i(\mathcal{D}_i, \mathcal{M}_i(\alpha_i, \beta, ...)), \tag{B2}$$

where \mathcal{D}_i is the spectra data in *i*-th time interval, $\mathcal{M}_i(\alpha_i, \beta, ...)$ represents the spectral model, α_i is a time-dependent parameter that varies freely across different time intervals, and β is a tied parameter for all intervals. The AIC and BIC values presented in Table B1 indicate that tying the temperatures for the plateau's time intervals can indeed slightly improve the acceptability of the model.

However, only with a single BB, there is always a significant dip within the energy range from ~ 20 to ~ 50 keV, as shown in Figure B2. In order to reduce these discrepancies between the spectral data and model, we further consider another two spectral models by invoking an extra spectral component, which is either another BB or a cyclotron resonant scattering feature (CRSF) absorption. Here, the CRSF with a Gaussian profile implemented as a multiplicative model is given by:

$$M(E) = \exp\left\{-\tau_{\text{CRSF}} \exp\left[-\frac{(E - E_{\text{cyc}})^2}{2\sigma^2}\right]\right\},\tag{B3}$$

where $E_{\rm cyc}$ is the central energy of the line in units of keV, σ is the line width, and $\tau_{\rm CRSF}$ is the optical depth at the line center. Following the same approach as above, the BB temperatures are tied for the time intervals in the plateau phase and the CRSF parameters are tied for all intervals. The results presented in Figure B2 show that that both of these scenarios can help to eliminate the dip around ~ 35 keV. Furthermore, the AIC and BIC values listed in Table B1 strongly suggest that the best fit can be provided by the BB + CRSF model. The flux data presented in the left panel of Figure 3 for Burst A is just obtained with this model.

Finally, we further apply the BB + CRSF model to fit the time-resolved spectra of all other selected bursts. In fact, we have also examined the other three spectral models, which are however disfavored by their AIC and BIC values as listed in Table B1. So, for simplicity, we do not present these alternative fitting results. Bursts B-E fittings with the BB + CRSF model are shown in Figure B3. These results demonstrate that the peaks of the time-resolved spectra can always be concentrated around a constant value, and the temporal evolution of the spectra is solely determined by the variation of the emission area. Figure 4 presents the derived fluxes and emission areas versus time. The comparison given in the middle panels of this figure further demonstrates that these spectrum-determining emission areas can agree well with the area variation curve derived from the eclipse modeling.

REFERENCES

Bissaldi, E., von Kienlin, A., Lichti, G., et al. 2009, Experimental Astronomy, 24, 47, doi: 10.1007/s10686-008-9135-4

Bochenek, C. D., Ravi, V., Belov, K. V., et al. 2020, Nature, 587, 59, doi: 10.1038/s41586-020-2872-x

Borghese, A., Coti Zelati, F., Israel, G. L., et al. 2022, MNRAS, 516, 602, doi: 10.1093/mnras/stac1314

Burns, E., Svinkin, D., Hurley, K., et al. 2021, ApJL, 907,L28, doi: 10.3847/2041-8213/abd8c8

Cai, C., Xue, W.-C., Li, C.-K., et al. 2022, ApJS, 260, 24, doi: 10.3847/1538-4365/ac6172

CHIME/FRB Collaboration, Andersen, B. C., Bandura, K. M., et al. 2020, Nature, 587, 54, doi: 10.1038/s41586-020-2863-y Collazzi, A. C., Kouveliotou, C., van der Horst, A. J., et al. 2015, ApJS, 218, 11, doi: 10.1088/0067-0049/218/1/11

Coti Zelati, F., Rea, N., Pons, J. A., Campana, S., & Esposito, P. 2018, MNRAS, 474, 961, doi: 10.1093/mnras/stx2679

Dall'Osso, S., La Placa, R., Stella, L., Bakala, P., & Possenti, A. 2024, ApJ, 973, 123, doi: 10.3847/1538-4357/ad5f1c

Duncan, R. C., & Thompson, C. 1992, ApJL, 392, L9, doi: 10.1086/186413

Goldstein, A., Cleveland, W. H., & Kocevski, D. 2022, Fermi GBM Data Tools: v1.1.1, https://fermi.gsfc.nasa.gov/ssc/data/analysis/gbm

- GöğüŞ , E., Woods, P. M., Kouveliotou, C., et al. 1999, ApJL, 526, L93, doi: 10.1086/312380
- Göğüş, E., Woods, P. M., Kouveliotou, C., et al. 2000, ApJL, 532, L121, doi: 10.1086/312583
- Harding, A. K., & Daugherty, J. K. 1991, ApJ, 374, 687, doi: 10.1086/170153
- He, J.-J., An, Z.-H., Peng, W.-X., et al. 2023, MNRAS, 525, 3399, doi: 10.1093/mnras/stad2439
- Ioka, K. 2020, ApJL, 904, L15,
 - doi: 10.3847/2041-8213/abc6a3
- Israel, G. L., Romano, P., Mangano, V., et al. 2008, ApJ, 685, 1114, doi: 10.1086/590486
- Israel, G. L., Esposito, P., Rea, N., et al. 2016, MNRAS, 457, 3448, doi: 10.1093/mnras/stw008
- Jones, P. B. 2003, ApJ, 595, 342, doi: 10.1086/377351
- Kaneko, Y., Göğüş, E., Baring, M. G., et al. 2021, ApJL, 916, L7, doi: 10.3847/2041-8213/ac0fe7
- Kaspi, V. M. 2010, Proceedings of the National Academy of Science, 107, 7147, doi: 10.1073/pnas.1000812107
- Kaspi, V. M., & Beloborodov, A. M. 2017, ARA&A, 55, 261, doi: 10.1146/annurev-astro-081915-023329
- Landau, L. D., & Lifshitz, E. M. 1980, Statistical physics. Pt.1, Pt.2
- Levin, Y., & Lyutikov, M. 2012, MNRAS, 427, 1574, doi: 10.1111/j.1365-2966.2012.22016.x
- Li, C. K., Lin, L., Xiong, S. L., et al. 2021, Nature Astronomy, 5, 378, doi: 10.1038/s41550-021-01302-6
- Li, X., & Beloborodov, A. M. 2015, ApJ, 815, 25, doi: 10.1088/0004-637X/815/1/25
- Li, X., Wen, X., An, Z., et al. 2021, Radiation Detection Technology and Methods, 6, 12, doi: 10.1007/s41605-021-00288-z
- Liddle, A. R. 2007, MNRAS, 377, L74, doi: 10.1111/j.1745-3933.2007.00306.x
- Lin, L., Göğüş, E., Roberts, O. J., et al. 2020a, ApJL, 902, L43, doi: 10.3847/2041-8213/abbefe
- Lin, L., Göğüş, E., Roberts, O. J., et al. 2020b, ApJ, 893, 156, doi: 10.3847/1538-4357/ab818f
- Lyubarsky, Y., Eichler, D., & Thompson, C. 2002, ApJL, 580, L69, doi: 10.1086/345402
- Masada, Y., Nagataki, S., Shibata, K., & Terasawa, T. 2010, PASJ, 62, 1093, doi: 10.1093/pasj/62.4.1093
- Meegan, C., Lichti, G., Bhat, P. N., et al. 2009, ApJ, 702, 791, doi: 10.1088/0004-637X/702/1/791
- Meng, Y., Lin, J., Zhang, L., et al. 2014, ApJ, 785, 62, doi: 10.1088/0004-637X/785/1/62
- Mereghetti, S. 2008, A&A Rv, 15, 225, doi: 10.1007/s00159-008-0011-z
- Mereghetti, S. 2013, Brazilian Journal of Physics, 43, 356, doi: 10.1007/s13538-013-0137-y

- Mereghetti, S., Rigoselli, M., Salvaterra, R., et al. 2024, Nature, 629, 58, doi: 10.1038/s41586-024-07285-4
- Meszaros, P., & Nagel, W. 1985, ApJ, 298, 147, doi: 10.1086/163594
- Negro, M., Younes, G., Wadiasingh, Z., et al. 2024, Frontiers in Astronomy and Space Sciences, 11, 1388953, doi: 10.3389/fspas.2024.1388953
- Nishimura, O. 2003, PASJ, 55, 849, doi: 10.1093/pasj/55.4.849
- Olausen, S. A., & Kaspi, V. M. 2014, ApJS, 212, 6, doi: 10.1088/0067-0049/212/1/6
- Olive, J. F., Hurley, K., Sakamoto, T., et al. 2004, ApJ, 616, 1148, doi: 10.1086/424957
- Parfrey, K., Beloborodov, A. M., & Hui, L. 2013, ApJ, 774, 92, doi: 10.1088/0004-637X/774/2/92
- Rehan, N. S., & Ibrahim, A. I. 2025, ApJS, 276, 60, doi: 10.3847/1538-4365/ad95f9
- Rehan, N. u. S., & Ibrahim, A. I. 2023, ApJ, 950, 121, doi: 10.3847/1538-4357/accae6
- Rehan, N. u. S., & Ibrahim, A. I. 2024, ApJ, 969, 38, doi: 10.3847/1538-4357/ad4635
- Ridnaia, A., Svinkin, D., Frederiks, D., et al. 2021, Nature Astronomy, 5, 372, doi: 10.1038/s41550-020-01265-0
- Roberts, O. J., Veres, P., Baring, M. G., et al. 2021, Nature, 589, 207, doi: 10.1038/s41586-020-03077-8
- Schönherr, G., Wilms, J., Kretschmar, P., et al. 2007, A&A, 472, 353, doi: 10.1051/0004-6361:20077218
- Stamatikos, M., Malesani, D., Page, K. L., & Sakamoto, T. 2014, GRB Coordinates Network, 16520, 1
- Thompson, C., & Blaes, O. 1998, PhRvD, 57, 3219, doi: 10.1103/PhysRevD.57.3219
- Thompson, C., & Duncan, R. C. 1995, MNRAS, 275, 255, doi: 10.1093/mnras/275.2.255
- Thompson, C., Duncan, R. C., Woods, P. M., et al. 2000, ApJ, 543, 340, doi: 10.1086/317072
- Thompson, C., Lyutikov, M., & Kulkarni, S. R. 2002, ApJ, 574, 332, doi: 10.1086/340586
- Trigg, A. C., Burns, E., Roberts, O. J., et al. 2024, A&A, 687, A173, doi: 10.1051/0004-6361/202348858
- Uzdensky, D. A. 2011, SSRv, 160, 45, doi: 10.1007/s11214-011-9744-5
- van der Horst, A. J., Kouveliotou, C., Gorgone, N. M., et al. 2012, ApJ, 749, 122, doi: 10.1088/0004-637X/749/2/122
- Wang, J. C. L., Wasserman, I., & Lamb, D. Q. 1993, ApJ, 414, 815, doi: 10.1086/173125
- Woods, P. M., Kouveliotou, C., Göğüş, E., et al. 2001, ApJ, 552, 748, doi: 10.1086/320571
- Woods, P. M., & Thompson, C. 2006a, in Compact stellar X-ray sources, ed. W. H. G. Lewin & M. van der Klis, Vol. 39, 547–586, doi: 10.48550/arXiv.astro-ph/0406133

Woods, P. M., & Thompson, C. 2006b, in Compact stellar X-ray sources, ed. W. H. G. Lewin & M. van der Klis, Vol. 39, 547–586, doi: 10.48550/arXiv.astro-ph/0406133

- Xiao, S., Xiong, S.-L., Cai, C., et al. 2022, MNRAS, 514, 2397, doi: 10.1093/mnras/stac999
- Xie, S.-L., Yu, Y.-W., Xiong, S.-L., et al. 2024, ApJ, 967, 108, doi: 10.3847/1538-4357/ad4093
- Xie, S.-L., Cai, C., Xiong, S.-L., et al. 2022, MNRAS, 517, 3854, doi: 10.1093/mnras/stac2918
- Xie, S.-L., Cai, C., Yu, Y.-W., et al. 2025, ApJS, 277, 5, doi: 10.3847/1538-4365/ada6a9
- Xue, W.-C., Xie, S.-L., Li, X.-B., & Xiong, S.-L. 2024, ELISA: Efficient Library for Spectral Analysis in High-Energy Astrophysics, v0.1.17 https://github.com/wcxve/elisa

- Yamasaki, S., Kashiyama, K., & Murase, K. 2022, MNRAS, 511, 3138, doi: 10.1093/mnras/stac234
- Yang, Y.-P., & Zhang, B. 2021, ApJ, 919, 89, doi: 10.3847/1538-4357/ac14b5
- Younes, G., Güver, T., Kouveliotou, C., et al. 2020, ApJL, 904, L21, doi: 10.3847/2041-8213/abc94c
- $Yu,\ C.\ 2011,\ ApJ,\ 738,\ 75,$
 - doi: 10.1088/0004-637X/738/1/75
- Yu, C., & Huang, L. 2013, ApJL, 771, L46, doi: 10.1088/2041-8205/771/2/L46
- Zhang, Z. J., Zhang, B.-B., & Meng, Y.-Z. 2023, MNRAS, 520, 6195, doi: 10.1093/mnras/stad443
- Zhong, S.-Q., Dai, Z.-G., Zhang, H.-M., & Deng, C.-M. 2020, ApJL, 898, L5, doi: 10.3847/2041-8213/aba262

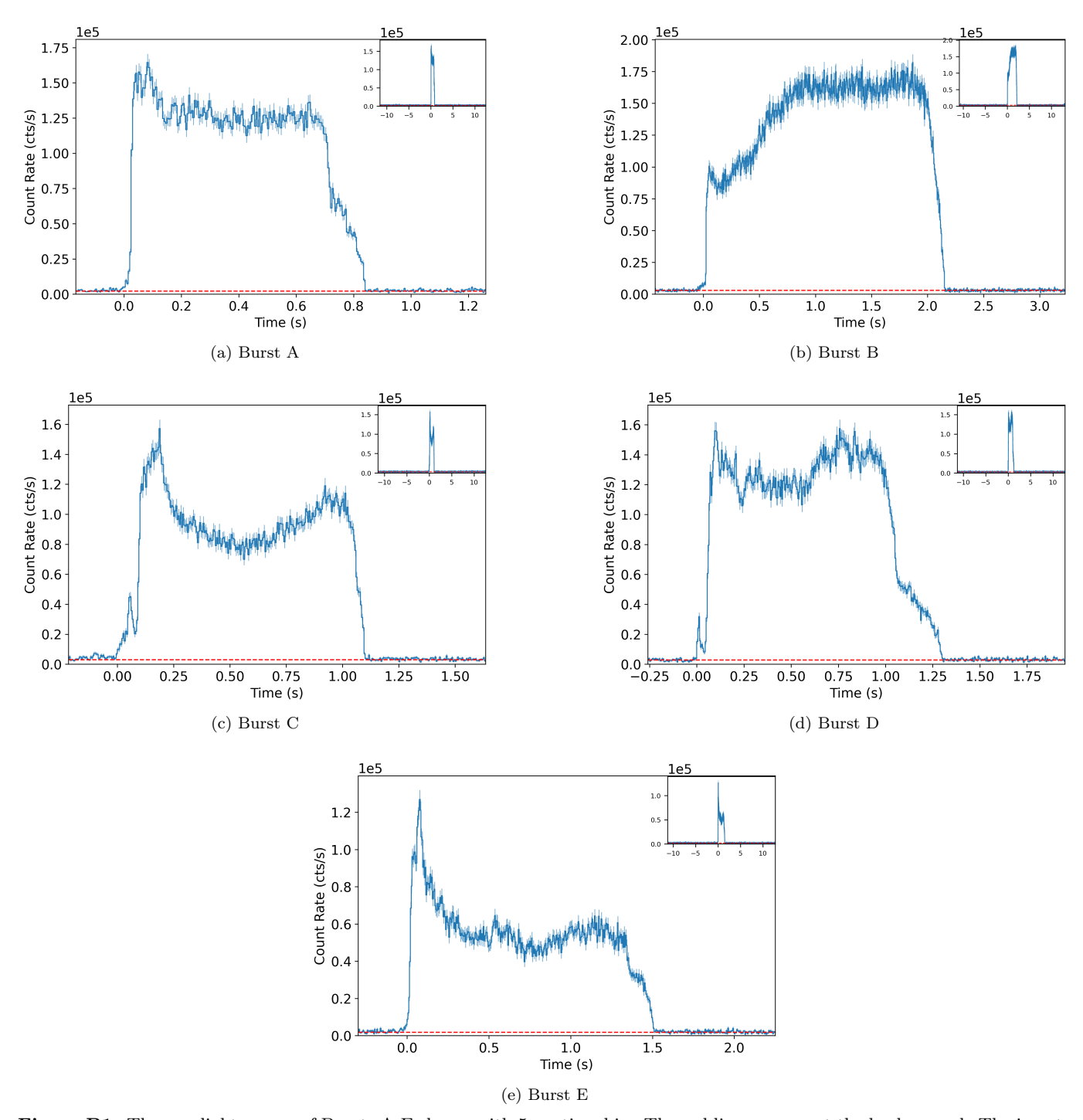


Figure B1. The raw light curves of Bursts A-E shown with 5 ms time bin. The red lines represent the background. The inserts show the light curves within a wider time range to illustrate the clean background level.

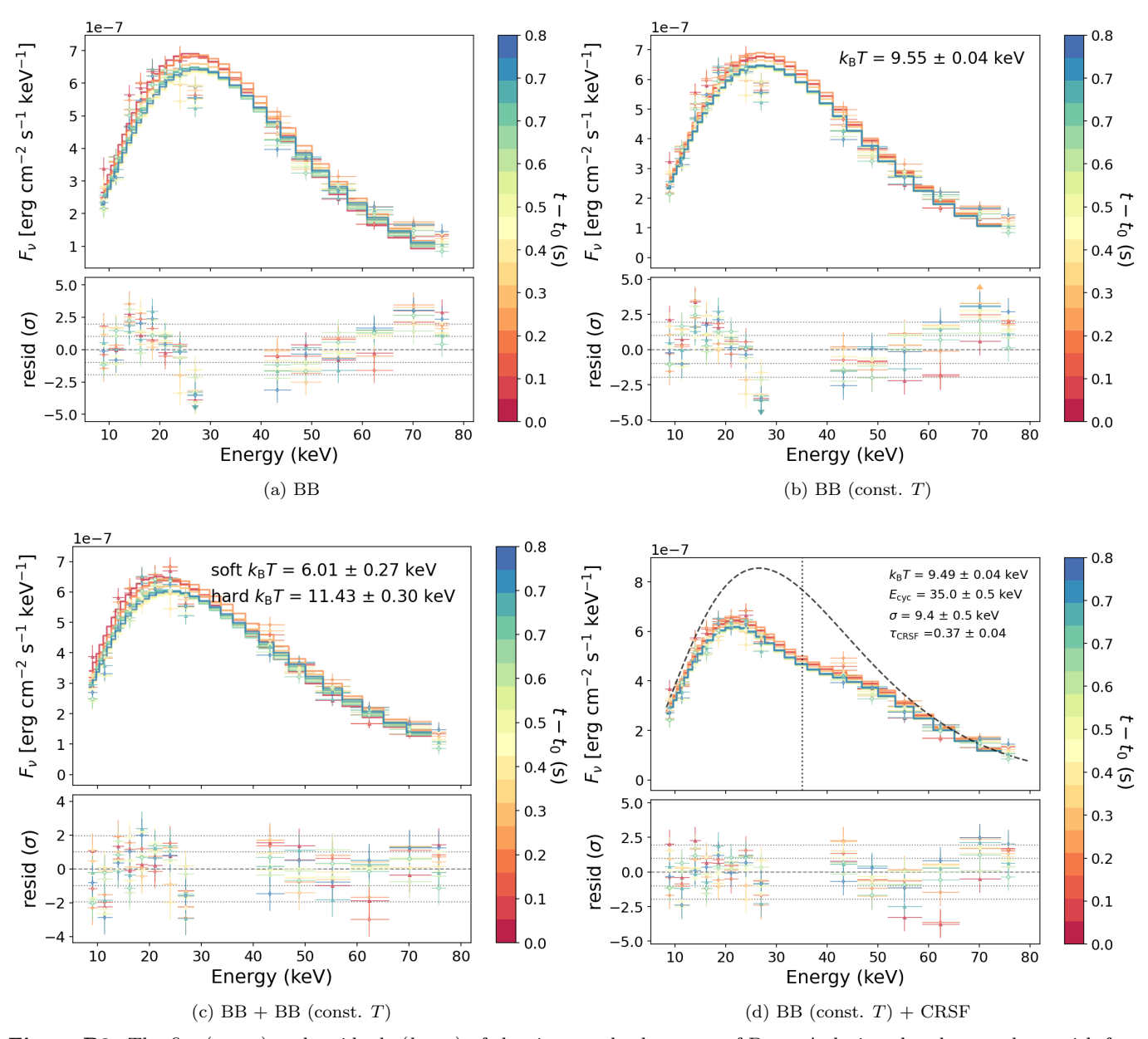


Figure B2. The fits (upper) and residuals (lower) of the time-resolved spectra of Burst A during the plateau phase with four different spectral models: (a) a single BB with free temperature, (b) a single BB with a constant temperature for all spectra, (c) double BB with constant temperatures, and (d) a single BB with constant temperature plus a CRSF. The dashed line given in panel d represent the BB spectrum without the CRSF absorption, where the emission area is taken to be the maximum one. The vertical dotted line represents the center of the CRSF ($E_{\rm cyc}$). In the constant temperature models, the difference between the spectra is solely determined by their different emission areas.

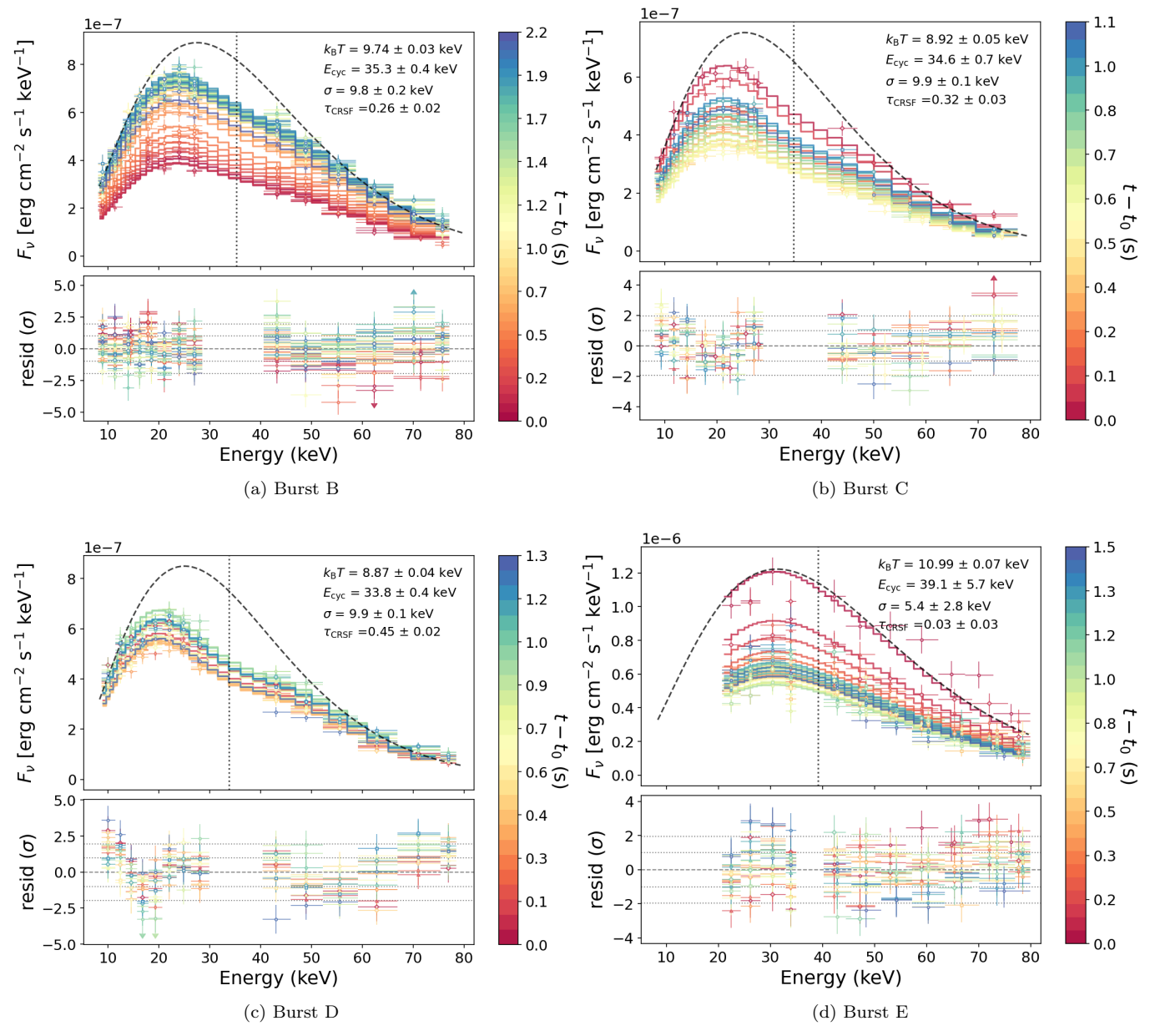


Figure B3. Same to the bottom right panel of Figure B2 but for Bursts B-E.

Table B1. The statistical goodness of the spectral fittings of Bursts A-E with four spectral models.

Burst	Model	χ^2/dof	AIC	BIC
A	BB	590.29/196	670.49	775.18
	BB (const. T)	601.29/206	655.14	731.80
	BB + BB (const. T)	293.96/182	415.95	554.99
	BB + CRSF (const. T)	316.99/203	378.48	463.82
В	BB	956.31/495	1158.60	1503.68
	BB (const. T)	1066.15/533	1170.99	1371.66
	BB + BB (const. T)	627.41/485	857.89	1238.42
	BB + CRSF (const. T)	715.28/530	827.31	1039.89
\mathbf{C}	BB	477.46/219	583.63	722.63
	BB (const. T)	499.33/236	559.76	649.78
	BB + BB (const. T)	253.90/209	390.46	554.80
	BB + CRSF (const. T)	329.48/233	397.50	496.64
D	BB	1278.93/299	1401.42	1583.69
	BB (const. T)	1308.46/316	1386.46	1513.58
	BB + BB (const. T)	359.09/281	534.59	769.34
	BB + CRSF (const. T)	590.72/313	676.22	813.43
Е	BB	345.00/262	493.05	691.47
	BB (const. T)	396.81/286	478.16	604.70
	BB + BB (const. T)	392.80/250	579.01	808.56
	BB + CRSF (const. T)	395.99/283	485.06	621.20